

GNSS Jamming Mitigation with a Pilot Signal Aided Deep Integration Framework

Kana Nagai, Samer Khanafseh, Boris Pervan, *Illinois Institute of Technology*

BIOGRAPHY

Kana Nagai is a Senior Research Associate in the Department of Mechanical and Aerospace Engineering at the Illinois Institute of Technology (IIT). She holds M.S. and Ph.D. degrees in Mechanical and Aerospace Engineering, as well as a B.S. in Mechanical Engineering, all from IIT. Additionally, she earned a Bachelor's degree in Architectural and Structural Design from Hokkaido University in Japan. Her research centers on assessing the navigation safety of autonomous vehicles operating in complex situations, such as urban environments and jamming conditions.

Samer Khanafseh is currently a research associate professor at Illinois Institute of Technology (IIT), Chicago, and the principal of TruNav LLC. He received his MSc and PhD degrees in Aerospace Engineering from IIT in 2003 and 2008, respectively. Dr. Khanafseh has been involved in several aviation applications such as Autonomous Airborne Refueling (AAR) of unmanned air vehicles, autonomous shipboard landing for NUCAS and JPALS programs, and Ground Based Augmentation System (GBAS). His research interests are focused on high accuracy and high integrity navigation algorithms, cycle ambiguity resolution, high integrity applications, fault monitoring, and robust estimation techniques. He was the recipient of the 2011 Institute of Navigation Early Achievement Award for his outstanding contributions to the integrity of carrier phase navigation systems.

Boris Pervan is a Professor and Frank Gunsaulus Faculty Fellow in Mechanical and Aerospace Engineering at the Illinois Institute of Technology (IIT), where he conducts research on high integrity navigation systems. Prior to joining the faculty at IIT, he was a spacecraft mission analyst at Hughes Aircraft Company (now Boeing) and a postdoctoral research associate at Stanford University. Prof. Pervan received his B.S. from the University of Notre Dame, M.S. from the California Institute of Technology, and Ph.D. from Stanford University. He has received the Samuel M. Burka and Johannes Kepler Awards from the Institute of Navigation (ION), IIT Sigma Xi Excellence in University Research Award, IIT University Excellence in Teaching Award, IEEE Aerospace and Electronic Systems Society M. Barry Carlton Award, RTCA William E. Jackson Award, Guggenheim Fellowship, and the Albert J. Zahm Prize in Aeronautics. He is a Fellow of the ION and IEEE and former Editor-in-Chief of the ION journal NAVIGATION.

ABSTRACT

This paper investigates whether tracking GNSS pilot signals using ultra-tight (deep) coupling with inertial sensors can significantly improve GNSS robustness under severe wideband jamming. Because GNSS pilot signals do not contain navigation-bit transitions, they enable longer coherent integration intervals. Increasing the coherent integration time averages down measurement noise and increases the effective signal-to-noise ratio, yielding more reliable measurements under low carrier-to-noise ratio (C/N_0) conditions. Ultra-tight coupling fuses correlator I/Q measurements with inertial data through an extended Kalman filter, reducing carrier-phase estimation error to enable the longer averaging intervals. However, simulations indicate that increasing the integration time reduces measurement noise while simultaneously increasing the accumulation of process noise due to inertial sensor random-walk errors. When this accumulated process noise exceeds a critical threshold, the receiver is unable to maintain lock, resulting in cycle slips. Thus, tracking robustness is ultimately constrained more by process-noise accumulation than by measurement-noise reduction, implying that longer coherent integration times do not necessarily improve robustness, but that selecting inertial sensors with low random walk error characteristics can.

I. INTRODUCTION

GNSS is critical infrastructure for modern positioning systems, yet it remains vulnerable to jamming, posing serious safety risks. Such interference degrades positioning accuracy and threatens system continuity. To address this vulnerability, augmentation and mitigation strategies are expected to enhance GNSS resilience to jamming.

Jamming refers to interference within the GNSS radio-frequency bands, typically transmitted at power levels far exceeding those of the inherently weak GNSS signals. Jammers can be categorized by the manner in which they inject energy into the GNSS band, including amplitude-modulated (AM) or continuous-wave (CW) jammers, frequency-modulated (FM) jammers, chirp (swept-frequency) jammers, pulse jammers, narrowband noise jammers, and wideband noise jammers (Morales Ferre et al., 2019). Wideband noise jammers, also referred to as broadband jammers, distribute noise power across much or all of the GNSS spectrum, thereby raising the receiver noise floor and reducing the carrier-to-noise density ratio (C/N_0). Each jammer class

exhibits distinct threat characteristics and requires different countermeasures. This paper focuses specifically on the wideband noise jammer threat.

Many anti-jamming methods have been developed to address wideband noise interference. One widely used approach is vector tracking, which shifts from per-channel DLL/PLL tracking to a centralized estimator that jointly estimates the navigation state. These state estimates are used to drive all tracking channels, reducing reliance on per-channel PLL discriminators, and improving tracking robustness (Lashley et al., 2009; Martin, 2023). The robustness of vector tracking depends on accurate state estimation, which is obtained by coupling GNSS with an inertial navigation system (INS) through a navigation filter, typically an extended Kalman filter (EKF).

Three coupling architectures are commonly employed: loosely coupled, tightly coupled, and ultra-tightly coupled integration. In a loosely coupled architecture, an INS/GNSS filter fuses GNSS-derived position and velocity solutions with INS measurements. In a tightly coupled architecture, the filter instead fuses raw GNSS observables—such as pseudorange and carrier phase—with INS measurements (Falco et al., 2017; Groves, 2013). In contrast, ultra-tightly coupled integration fuses either GNSS receiver discriminator outputs or correlator in-phase (I) and quadrature (Q) outputs directly with INS measurements and is often referred to as deep integration (Watts and Martin, 2022; Jwo et al., 2012).

Our primary mitigation strategy is the use of GNSS pilot signals (e.g., GPS L5) to counter the elevated receiver noise floor under wideband jamming. Because pilot channels contain no navigation-bit transitions, they avoid unpredictable phase inversions and support coherent integration times substantially longer than the 20 ms limit of the GPS L1 C/A signal (Pany et al., 2009). During coherent integration, the correlator multiplies the incoming signal by a local replica and accumulates the result to form prompt I/Q outputs. This process allows the signal component to accumulate while random noise averages down, thereby improving the effective signal-to-noise ratio and yielding cleaner measurements. However, extending the integration interval also allows IMU- and clock-driven process errors to grow. As these errors accumulate, the local replica may gradually lose alignment with the incoming signal during integration, resulting in drift.

In this work, we identify the primary causes of carrier-phase tracking loss, analyze GNSS measurement and IMU selection for ultra-tightly coupled EKF tracking to reduce phase error, and exploit GNSS pilot signals—illustrated using GPS L5—to enable longer coherent integration that averages down measurement noise. Finally, through simulation, we assess whether coherent integration of pilot signals combined with inertial-aided vector tracking can enhance GNSS robustness under severe jamming.

The remainder of this paper is organized as follows. Section II introduces the jammer threat model. Section III describes correlator I/Q measurement formation, and Section IV presents centralized phase estimation. Section V discusses phase-tracking failure and the underlying mechanisms. Section VI presents Monte Carlo simulation results. Section VII concludes the paper and summarizes the main findings.

II. JAMMER THREAT MODEL FOR GPS L5 SIGNALS

We begin by introducing a jammer threat model that characterizes the interference and describes how a jammer can act on the target receiver. In the presence of interference, the received complex baseband signal can be modeled as

$$r(t) = g(t) + J(t) + s(t) + n(t), \quad (1)$$

where

$$\begin{aligned} g(t) &: \text{GNSS signal,} \\ J(t) &: \text{jamming signal,} \\ s(t) &: \text{spoofing signal (assumed zero here, i.e., } s(t) = 0), \\ n(t) &: \text{receiver thermal noise.} \end{aligned}$$

For a wideband noise jammer, the interference term is modeled as

$$J(t) = \sqrt{P_J} w_J(t), \quad w_J(t) \sim \mathcal{CN}(0, 1), \quad (2)$$

where P_J is the jammer power and $w_J(t)$ is zero-mean, unit-variance, white complex Gaussian noise (Morales Ferre et al., 2019). Because broadband jamming behaves approximately as white Gaussian noise in baseband, our countermeasures focus on reducing the effective white-noise level. Under the assumptions of no spoofing and a wideband noise jammer, we therefore model the jammer as an additive noise term combined with the receiver's thermal noise:

$$\tilde{n}(t) \equiv n(t) + J(t) \sim \mathcal{CN}(0, \sigma_n^2 + P_J). \quad (3)$$

Then the received signal model becomes

$$r(t) = g(t) + \tilde{n}(t), \quad (4)$$

where $g(t)$ is the sum of the GNSS signals from all visible satellites:

$$g(t) = \sum_{s \in \mathcal{S}} g_s(t). \quad (5)$$

A single-satellite GNSS pilot signal at complex baseband can be written as

$$g_s(t) = \sqrt{A} C(t - \tau) e^{j(2\pi f_D t + \phi)}, \quad (6)$$

where

- A : received carrier power,
- $C(t - \tau)$: PRN spreading code delayed by code phase τ ,
- f_D : residual carrier Doppler at complex baseband,
- ϕ : residual carrier phase.

We define in-phase and quadrature components by $r(t) \triangleq I(t) + j Q(t)$.

III. CORRELATOR I/Q MEASUREMENT FORMATION

1. Replica Generation

The received complex baseband signal is correlated with a local replica and coherently summed over the integration interval T_{coh} at the sampling rate f_s . This causes signal components to add linearly, while the zero-mean noise averages toward zero. As a result, coherent integration increases the signal amplitude relative to the noise.

To describe the coherent integration process in discrete time, we use two time scales: a slow coherent-interval index n and a fast sample index k (see Fig. 1). The index k runs over the samples inside the interval n (e.g., $k = 0, \dots, K - 1$ with $K = T_{\text{coh}} f_s$), and it resets to $k = 0$ at the start of the next interval $n + 1$.

The replica code phase in units of chips can be described as

$$\hat{\theta}_{n,k} = \hat{f}_{\text{chip},n} (t_{n,k} - \hat{\tau}_n), \quad \text{with} \quad f_{\text{chip},n} = f_{\text{code}} \left(1 + \frac{\hat{f}_{D,n}}{f_L} \right), \quad t_{n,k} = t_n + \frac{k}{f_s}, \quad (7)$$

where

- $\hat{\theta}_{n,k}$: estimated code phase at time $t_{n,k}$,
- $\hat{f}_{\text{chip},n}$: estimated code chip rate during the interval,
- $t_{n,k}$: within-interval sample time at index k ,
- $\hat{\tau}_n$: estimated code delay at the start of the interval,
- f_{code} : nominal code rate (e.g., 10.23 Mcps for GPS L5),
- $\hat{f}_{D,n}$: estimated Doppler at the start of the interval,
- f_L : nominal carrier frequency (e.g., 1176.45 MHz for GPS L5).

The replica carrier phase in radians at complex baseband is given by

$$\hat{\phi}_{n,k} = \hat{\phi}_n + 2\pi \hat{f}_{D,n} (t_{n,k} - t_n). \quad (8)$$

where

- $\hat{\phi}_{n,k}$: estimate of the replica carrier phase at time $t_{n,k}$,
- $\hat{\phi}_n$: posterior carrier phase at the start of the interval n .

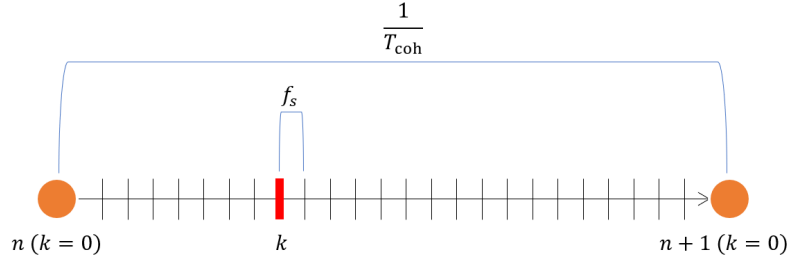


Figure 1: Discrete-time view of coherent integration. Each coherent integration interval has duration T_{coh} and is indexed by the slow-time counter n and the fast-time sample counter k . The index k runs over the samples inside the interval (e.g., $k = 0, \dots, K - 1$ with $K = T_{\text{coh}}f_s$), and it resets to $k = 0$ at the start of the next interval $n + 1$.

2. Correlation and Coherent Integration

The generated replica signals are then correlated with the incoming signal and coherently integrated over the coherent integration time, defined as

$$Z_{P,n} \triangleq \int_{t_n}^{t_n + T_{\text{coh}}} r(t) C(t - \hat{\tau}_n) e^{-j(2\pi \hat{f}_{D,n} t + \hat{\phi}_n)} dt. \quad (9)$$

This produces prompt correlator outputs, which for a single satellite evaluate to

$$I_{P,n} = \sqrt{A} R_C(\Delta\tau_n) \text{sinc}(\pi \Delta f_n T_{\text{coh}}) \cos(\Delta\phi_n) + n_{I,n}, \quad (10)$$

$$Q_{P,n} = \sqrt{A} R_C(\Delta\tau_n) \text{sinc}(\pi \Delta f_n T_{\text{coh}}) \sin(\Delta\phi_n) + n_{Q,n}. \quad (11)$$

where

$R_C(\Delta\tau_n)$: normalized code autocorrelation function,

$\Delta\tau_n$: code-delay error, $\Delta\tau_n \triangleq \tau_n - \hat{\tau}_n$,

Δf_n : Doppler frequency error, $\Delta f_n \triangleq f_{D,n} - \hat{f}_{D,n}$,

$\Delta\phi_n$: carrier-phase error, $\Delta\phi_n \triangleq \phi_n - \hat{\phi}_n$,

$n_{I,n}, n_{Q,n}$: zero-mean Gaussian noise.

The in-phase and quadrature noise variances are

$$\sigma_{n_I}^2 = \sigma_{n_Q}^2 = \frac{1}{2T_{\text{coh}} 10^{(C/N_0)/10}} \quad (12)$$

where C/N_0 is in dB-Hz (Parkinson and Spilker, 1996).

If carrier tracking is accurate, the residual Doppler error is negligible, $\text{sinc}(\pi \Delta f T_{\text{coh}}) = 1$ and

$$I_{P,n} = \sqrt{A} R_C(\Delta\tau_n) \cos(\Delta\phi_n) + n_{I,n}, \quad (13)$$

$$Q_{P,n} = \sqrt{A} R_C(\Delta\tau_n) \sin(\Delta\phi_n) + n_{Q,n}. \quad (14)$$

Since $Z_{P,n}$ is formed by integrating over T_{coh} , the desired signal component accumulates coherently over the interval, whereas the zero-mean noise averages down, reducing its variance in proportion to $1/T_{\text{coh}}$. Clearly a longer coherent integration time reduces the measurement noise.

IV. CENTRALIZED PHASE ESTIMATION

1. Navigation-state aiding for code/carrier NCOs

Many anti-jamming methods have been developed, and prior studies have shown that ultra-tightly coupled GNSS/INS integration with vector tracking can maintain robust tracking under wideband noise jamming (Lashley et al., 2009; Martin, 2023; Falco et al., 2017; Groves, 2013; Watts and Martin, 2022; Jwo et al., 2012). Figure 2 illustrates the ultra-tightly coupled architecture used in this paper. The receiver samples the baseband signal at a high rate, generates local replicas, and performs correlation followed by coherent integration to produce prompt in-phase and quadrature measurements. These outputs are fed directly into an EKF as measurement updates. In parallel, the INS provides inertial measurements (i.e., specific forces and angular rates), which the EKF uses for time propagation.

The key idea of vector tracking is that the EKF produces centralized state estimates that are used to drive each channel's code and carrier numerically controlled oscillators (NCOs). Thus, instead of independent per-channel PLL/DLL tracking loops, the receiver applies shared, navigation-state-based predictions across all channels. The filter fuses correlator measurements from all tracked satellites to jointly estimate receiver states and per-satellite dynamics, and it predicts code delay and carrier phase. These predictions directly control each channel's NCOs and therefore the locally generated replicas.

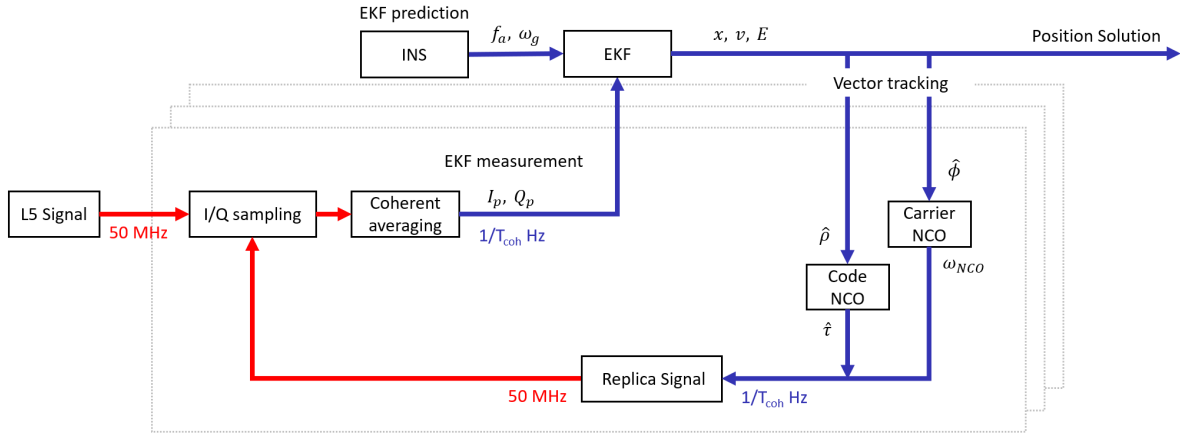


Figure 2: Block diagram of our ultra-tightly coupled with vector tracking architecture, where the navigation filter jointly estimates receiver states and predicts per-satellite code delay and carrier phase.

We derive the equations that map the EKF state estimates to per-satellite code and carrier replica parameters. An initial code delay $\tau_n \triangleq \tau_{n,0}$ in (7) for a satellite at interval n is

$$\tau_n = \frac{1}{c} (\rho_n + I_n + T_n + c\delta t_{r,n} - c\delta t_{s,n}) \quad (15)$$

where

- ρ : geometric range,
- I : ionospheric delay along the line of sight,
- T : tropospheric delay,
- $c\delta t_r$: receiver clock bias,
- $c\delta t_s$: satellite clock bias.

The geometric range is

$$\rho = \|\mathbf{r}_s - \mathbf{r}_r\| \quad (16)$$

where

- \mathbf{r}_s : satellite position vector,
- \mathbf{r}_r : receiver position vector.

If ionospheric and tropospheric delays are neglected (as they change very slowly relative to phase tracking dynamics) and we

ignore the satellite clock error for the moment, the code delay simplifies to

$$\tau_n = \frac{1}{c} (\rho_n + c \delta t_{r,n}). \quad (17)$$

An initial carrier phase for a satellite at interval n is

$$\phi_n = \frac{2\pi}{\lambda_L} \rho_n + 2\pi f_L \delta t_{r,n} + 2\pi N_n. \quad (18)$$

where $\lambda_L = c/f_L$ and N_n is the integer cycle ambiguity. The integer ambiguity is not relevant in generating the local replica and during tracking so it can be ignored.

The replica errors $\Delta\tau_n$ and $\Delta\phi_n$ can be described as:

$$\Delta\tau_n = \frac{1}{c} \mathbf{e}^{*T} \delta \mathbf{r}_n + \Delta t_{r,n}. \quad (19)$$

$$\Delta\phi_n = \frac{2\pi}{\lambda_L} (\mathbf{e}^{*T} \delta \mathbf{r}_n + c \Delta t_{r,n}). \quad (20)$$

where

$$\mathbf{e}^* \triangleq \frac{\mathbf{r}_s - \mathbf{r}_r^*}{\|\mathbf{r}_s - \mathbf{r}_r^*\|},$$

$$\Delta t_{r,n} \triangleq \delta t_{r,n} - \hat{\delta} t_{r,n},$$

$(\cdot)^*$ represent nominal values at the prompt-correlator epoch, and $\delta \mathbf{r}_n$ is defined below.

2. Ultra-tightly coupled EKF with correlator I/Q and inertial aiding

The receiver's position \mathbf{r}_n is obtained from the INS/GNSS EKF navigation solution. The INS continuous-time linearized error-state model is given by:

$$\underbrace{\begin{bmatrix} \delta \dot{\mathbf{r}} \\ \delta \dot{\mathbf{v}} \\ \delta \dot{\mathbf{E}} \\ \dot{\mathbf{b}}_a \\ \dot{\mathbf{b}}_g \\ c \delta \dot{t}_r \\ c \delta \dot{t}_d \end{bmatrix}}_{\dot{\mathbf{x}}_n} = \mathbf{F}_n \underbrace{\begin{bmatrix} \delta \mathbf{r} \\ \delta \mathbf{v} \\ \delta \mathbf{E} \\ \mathbf{b}_a \\ \mathbf{b}_g \\ c \delta t_r \\ c \delta t_d \end{bmatrix}}_{\mathbf{x}_n} + \mathbf{G}_{u,n} \underbrace{\begin{bmatrix} \delta \tilde{\mathbf{f}}_B^I \\ \delta^I \tilde{\boldsymbol{\omega}}_B^B \end{bmatrix}}_{\mathbf{u}_n} + \mathbf{G}_{w,n} \underbrace{\begin{bmatrix} \nu_a \\ \nu_g \\ \eta_a \\ \eta_g \\ S_b \\ S_r \end{bmatrix}}_{\mathbf{w}_n} \quad (21)$$

where

- $\delta \mathbf{r}$: receiver position error in navigation frame (N),
- $\delta \mathbf{v}$: receiver velocity error in N ,
- $\delta \mathbf{E}$: receiver attitude error in N ,
- \mathbf{b}_a : accelerometer bias,
- \mathbf{b}_g : gyroscope bias,
- $c \delta t_r$: receiver clock bias,
- $c \delta t_d$: receiver clock drift,
- $\delta \tilde{\mathbf{f}}_B^I$: specific-force measurement residual in body frame (B),
- $\delta^I \tilde{\omega}_B^B$: angular-rate measurement residual in B ,
- ν_a : accelerometer random walk,
- ν_g : gyro random walk,
- η_a : accelerometer bias stability,
- η_g : gyro bias stability,
- S_b : clock bias noise,
- S_r : clock drift noise.

Details of the matrices \mathbf{F} , \mathbf{G}_u , \mathbf{G}_w , and noise model are provided in Nagai et al. (2024).

From equations (13), (14), (19), and (20), the single-satellite prompt correlator measurements are:

$$I_P = K R_C(\Delta\tau) \cos(\Delta\phi) + n_I, \quad (22)$$

$$Q_P = K R_C(\Delta\tau) \sin(\Delta\phi) + n_Q, \quad (23)$$

where $K \triangleq \sqrt{A}$, and

$$\Delta\tau = \frac{1}{c} \mathbf{e}^{*T} \delta \mathbf{r} + \Delta t_r, \quad (24)$$

$$\Delta\phi = \frac{2\pi}{\lambda_L} \left(\mathbf{e}^{*T} \delta \mathbf{r} + c \Delta t_r \right). \quad (25)$$

Linearized at the prompt-correlator epoch and stacked over all satellites, the measurements yield the EKF measurement model. For clarity, we present a reduced measurement mapping showing only the position and velocity EKF states.

$$\underbrace{\begin{bmatrix} I_P - I_P^* \\ Q_P - Q_P^* \end{bmatrix}}_{z_n} = \underbrace{\begin{bmatrix} \frac{\partial I_P}{\partial \delta \mathbf{r}} |_* & 0 \\ \frac{\partial Q_P}{\partial \delta \mathbf{r}} |_* & 0 \end{bmatrix}}_{H_n} \underbrace{\begin{bmatrix} \delta \mathbf{r} \\ \delta \mathbf{v} \end{bmatrix}}_{x_n} + \underbrace{\begin{bmatrix} v_i \\ v_q \end{bmatrix}}_{v_n} \quad (26)$$

where

$$\begin{aligned} \frac{\partial I_P}{\partial \delta \mathbf{r}} &= K R'_C(\Delta\tau^*) \cos(\Delta\phi^*) \frac{1}{c} \mathbf{e}^{*T} - K R_C(\Delta\tau^*) \sin(\Delta\phi^*) \frac{2\pi}{\lambda} \mathbf{e}^{*T}, \\ \frac{\partial Q_P}{\partial \delta \mathbf{r}} &= K R'_C(\Delta\tau^*) \sin(\Delta\phi^*) \frac{1}{c} \mathbf{e}^{*T} + K R_C(\Delta\tau^*) \cos(\Delta\phi^*) \frac{2\pi}{\lambda} \mathbf{e}^{*T}. \end{aligned}$$

The prompt-correlator accumulation noises are assumed zero-mean Gaussian, $\mathcal{N}(\mathbf{0}, \mathbf{R}_n)$, where for a single satellite the measurement-noise covariance is

$$\mathbf{R}_n = \begin{bmatrix} \sigma_{n_I}^2 & 0 \\ 0 & \sigma_{n_Q}^2 \end{bmatrix}.$$

We discretize the continuous-time model over and apply an EKF with prediction and measurement update at each coherent interval $n T_{\text{coh}}$.

3. Fisher-Information analysis for GNSS measurements

To support our choice of an ultra-tightly coupled design for anti-jamming tracking, we briefly compare three common INS/GNSS coupling architectures (Table 1). Prior research suggests that ultra-tightly coupled integration offers superior performance, while loosely coupled integration performs the worst (Jwo et al., 2012; Martin, 2023; Niu et al., 2015). To verify this, we quantify how much information each architecture can retain using the Fisher information matrix (see appendix), which characterizes the certainty of the state estimate. A higher Fisher information value indicates greater confidence in the estimate.

Table 1: Coupling architectures

Fusion Architecture	GNSS measurement
Loosely coupled	GNSS position/velocity/time from receiver
Tightly coupled	Per-satellite pseudorange, Doppler, and carrier phase
Ultra-tightly coupled (discriminator)	Per-channel discriminator outputs
Ultra-tightly coupled (correlator)	Correlator I/Q from tracking channels

Following the equation in Bar-Shalom et al. (2001), and assuming a constant measurement rate with fixed measurement matrix H and noise covariance matrix V , the per-epoch Fisher information is given by

$$F = H^T V^{-1} H. \quad (27)$$

The details of the H and V matrices are provided in the appendix. To simplify the comparison, we define the score as

$$I = \det(F). \quad (28)$$

Table 2 summarizes the comparison, using eight GPS satellites at 45 dB-Hz, showing that the ultra-tightly coupled architecture retains more information than the other coupling architectures. This suggests that it enables more accurate position estimates and, consequently, reduces phase-tracking error.

Table 2: Fisher information for different coupling architectures, using eight GPS satellites at 45 dB-Hz.

Coupling architecture	$\det(F)$
Ultra-tightly coupled (discriminator and correlator)	5.55×10^{18}
Tightly coupled	2.19×10^{14}
Loosely coupled	1.00×10^0

4. IMU quality and steady-state phase error

The steady-state error covariance is obtained by solving the discrete-time algebraic Riccati, given by

$$\Phi \bar{P}_\infty \Phi^T - \bar{P}_\infty - \Phi \bar{P}_\infty H^T (H \bar{P}_\infty H^T + V)^{-1} (\Phi \bar{P}_\infty H^T)^T + Q = 0 \quad (29)$$

where

- Φ : discrete-time state-transition matrix,
- \bar{P}_∞ : steady-state *a priori* (predicted) error covariance,
- H : measurement matrix,
- V : measurement noise covariance matrix,
- Q : process-noise covariance matrix (per epoch).

This yields the expected EKF position error for a given IMU error model and measurement noise level. Table 3 summarizes results for an ultra-tightly coupled architecture using eight GPS satellites at 0 dB-Hz. Across the selected IMUs, from navigation-grade to consumer-grade, the one-sigma steady-state position error remains small, between 9 and 15 mm. These results indicate that the IMU “grade” label alone is not a reliable predictor of steady-state performance. Instead, the IMU noise parameters, particularly the *random-walk* terms, dominate the steady-state position error by driving process-noise growth during propagation.

Table 3: Steady-state position error and representative IMU noise parameters, using eight GPS satellites at 0 dB-Hz.

IMU	Steady State Error	Grade	Random Walk		Bias Stability	
	1σ , m		Velo. m/s/ $\sqrt{\text{hr}}$	Angular deg/ $\sqrt{\text{hr}}$	Acc. milli-g	Gyro deg/hr
1	0.009	Navigation	0.018	0.005	0.1	0.05
2	0.013	Tactical	0.008	0.09	0.0036	1.8
3	0.014	Industrial	0.014	0.15	0.0044	2.7
4	0.015	Tactical	0.07	0.15	0.05	0.5
5	0.015	Consumer	0.04	0.17	0.3	4.5

V. PHASE-TRACKING FAILURE EVALUATION AND MECHANISM

So far, we have discussed how to improve estimation accuracy and reduce measurement noise; here, we explain how to evaluate tracking robustness and how these factors are directly linked to the mechanisms that cause loss of lock. A loss of phase tracking occurs when the receiver can no longer follow the incoming carrier, leading to a discontinuity in the phase estimate. We quantify this behavior using the carrier-phase error

$$\Delta\phi(t) \triangleq \phi(t) - \hat{\phi}(t), \quad (30)$$

where $\phi(t)$ is the true carrier phase and $\hat{\phi}(t)$ is the estimated carrier phase. Immediately after jamming onset, the phase error remains close to zero, indicating stable phase tracking. However, when phase tracking is lost, the phase error exhibits an abrupt jump. After this event, the error typically remains offset by an approximately integer number of cycles (a cycle ‘slip’), which corrupts carrier-phase navigation.

To understand why loss of phase tracking occurs, we examine the phase-error dynamics, described by the following equation (Spilker, 1977):

$$\Delta\dot{\phi}(t) = -K[A \sin(\Delta\phi(t)) + n_a(t)] \quad (31)$$

where

- $\Delta\phi(t)$: carrier-phase error,
- K : loop gain,
- A : signal amplitude,
- $n_a(t)$: additive disturbance term (e.g., measurement-noise).

The phase-error dynamics are captured by a nonlinear differential equation with (i) a stabilizing feedback term that drives the error toward a stable equilibrium and (ii) disturbance terms due to measurement noise. Figure 3 illustrates how the carrier-phase error evolves over time. The blue vector field represents the restoring behavior induced by the nonlinear term (e.g., the sine term). At small phase errors, they converge toward the stable equilibrium over time. However, sufficiently large disturbances arising from measurement noise and accumulated process noise can push the phase error beyond the stability boundary (approximately ± 180 degrees), after which the estimator converges to an adjacent equilibrium and a cycle slip occurs. Equation (31) shows that the loss of tracking happens due to (i) carrier phase error from inaccurate estimation, and (ii) elevated measurement noise under low C/N_0 .

VI. SIMULATION SETUP AND RESULTS

A simulation is conducted at a severe jamming level ($C/N_0 = 5$ dB-Hz) while sweeping the coherent integration time T_{coh} from 1 ms to 5 s. For each T_{coh} , 100 Monte Carlo trials are performed. The receiver model uses an ultra-tightly coupled architecture that feeds correlator I/Q measurements into a vector-tracking EKF with a simple phase–frequency state model, and the analysis is restricted to a single satellite. A tactical-grade IMU (ADIS16490) and a rubidium clock are assumed for inertial and timing inputs. A cycle slip is declared when the carrier-phase error exceeds $\pm\pi$ radians.

Figure 4 presents the results, where each colored trace corresponds to one trial. The left plot shows the short coherent integration case ($T_{\text{coh}} = 10$ ms). In this regime, the phase error remains tightly bounded around zero over time, indicating stable phase lock across all trials. In contrast, the right plot shows a long coherent-integration case ($T_{\text{coh}} = 5$ s). Here, multiple trials exhibit abrupt phase discontinuities, consistent with loss of phase tracking and cycle slips.

Figure 5 summarizes the Monte Carlo results as a function of coherent integration time T_{coh} . The horizontal axis shows T_{coh} (s) and the vertical axis shows the carrier-phase tracking error. The blue markers report the Monte Carlo root-mean-square (RMS)

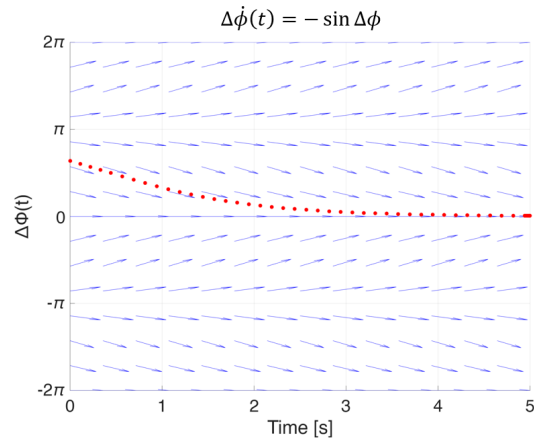


Figure 3: Phase-error dynamics in the nonlinear tracking model. The blue vector field illustrates the local phase-error flow induced by the restoring feedback term, and the red markers show a representative phase-error trajectory converging toward the stable equilibrium over time.

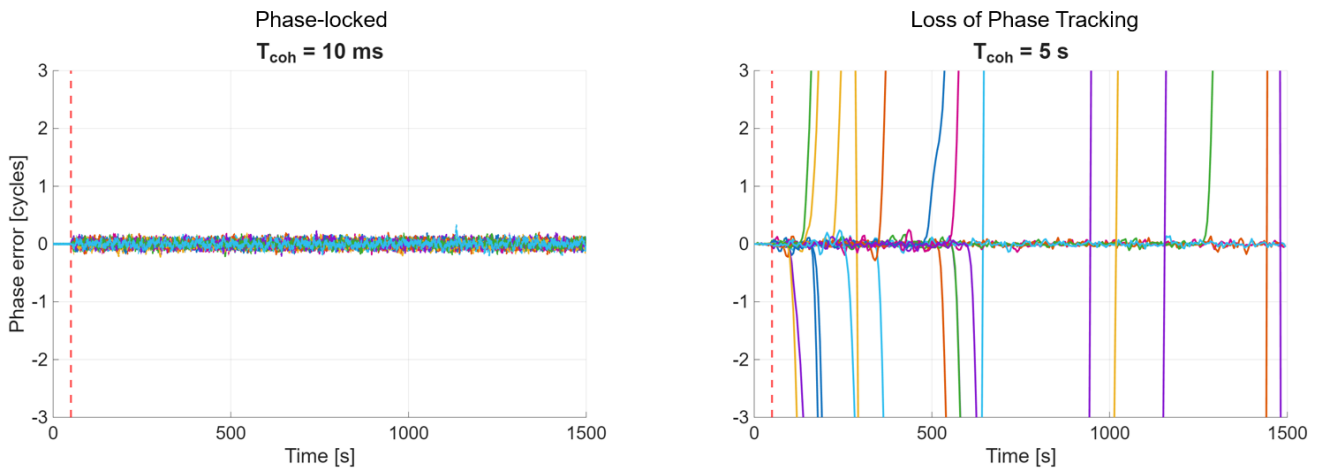


Figure 4: Monte Carlo examples of carrier-phase error under severe jamming ($C/N_0 = 5 \text{ dB-Hz}$). Left: short coherent integration. Right: long coherent integration.

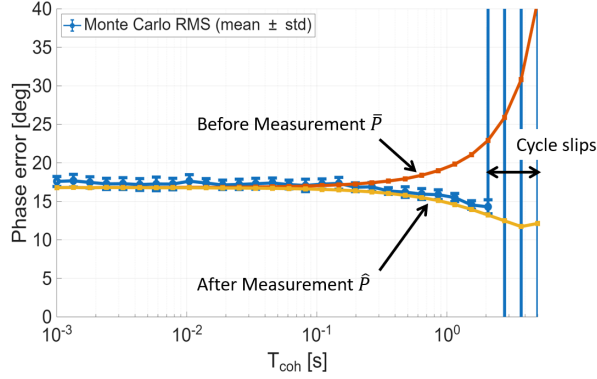


Figure 5: Monte Carlo carrier-phase error versus coherent integration time under severe jamming ($C/N_0 = 5$ dB-Hz), showing RMS phase error (blue) along with EKF (1σ) pre-update uncertainty from (\bar{P}) (red) and post-update uncertainty (\hat{P}) (yellow), where cycle slips occur at long (T_{coh}) as the propagated uncertainty grows.

phase error. The red curve shows the 1σ values derived from the EKF *a priori* covariance (before the measurement update), while the yellow curve shows the corresponding 1σ values from the EKF *a posteriori* covariance (after the measurement update).

For short to intermediate coherent integration times, the phase error remains bounded and cycle slips are not observed. However, when T_{coh} becomes excessively long (approximately > 2 s), a sharp degradation occurs and cycle slips become frequent. This behavior is explained by the competing effects of longer coherent integration on the EKF error covariance. As T_{coh} increases, coherent averaging reduces measurement noise, which improves the the posteriori uncertainty (the covariance *after* the measurement update). At the same time, a longer integration interval increases the accumulation of process disturbances (e.g., inertial and clock random walk errors) during propagation, which inflates the priori uncertainty (the covariance *before* the measurement update). Once the priori uncertainty exceeds a critical level, the phase estimate exits the stable region of the nonlinear phase dynamics, resulting in loss of lock and cycle slips. The key implication is that tracking robustness is governed primarily by the growth of the propagated uncertainty rather than by the reduction in measurement noise; therefore, increasing T_{coh} does not necessarily improve robustness under severe jamming in a tightly-coupled architecture.

VII. CONCLUSION

Coherent integration of GNSS pilot channels and GNSS/INS ultra-tightly coupled vector tracking can sustain carrier-phase tracking under severe wideband jamming. Pilot signals enable long coherent integration, which improves correlator I/Q measurement quality by averaging down noise; however, increasing T_{coh} also lengthens the propagation interval, allowing IMU- and clock-driven process disturbances to accumulate. Monte Carlo results show bounded phase error and no cycle slips for short-to-intermediate T_{coh} , but excessively long integration (about > 2 s) triggers a sharp degradation and frequent cycle slips. This transition is captured by the EKF covariance behavior: the post-measurement update uncertainty decreases with cleaner measurements, while the propagated pre-measurement update uncertainty grows with process-noise accumulation. Loss of lock becomes inevitable once the propagated uncertainty exceeds a critical level. Overall, the results indicate that robustness is limited by process-driven uncertainty growth rather than measurement-noise reduction, so longer coherent integration is not inherently beneficial under severe jamming.

APPENDIX: FISHER INFORMATION MODELS

This appendix summarizes the Fisher information models used in Table II for the ultra-tightly coupled, tightly coupled, and loosely coupled architectures.

A. Ultra-tightly coupled model

The state vector for the ultra-tightly coupled case is the receiver position error

$$\mathbf{x} = \delta \mathbf{r} \in \mathbb{R}^3.$$

For m tracked satellites, the measurement vector consists of two correlator outputs per satellite,

$$\mathbf{z}_{\text{ultra}} = [z_{1,I} \quad z_{1,Q} \quad \cdots \quad z_{m,I} \quad z_{m,Q}]^T \in \mathbb{R}^{2m}.$$

Let $\mathbf{e}_i \in \mathbb{R}^3$ denote the unit line-of-sight vector from the receiver to satellite i , and define the stacked line of the sight matrix

$$E \triangleq \begin{bmatrix} \mathbf{e}_1^T \\ \vdots \\ \mathbf{e}_m^T \end{bmatrix} \in \mathbb{R}^{m \times 3}.$$

The measurement Jacobian is

$$H_{\text{ultra}} = \begin{bmatrix} -\frac{1}{c}E \\ \frac{c}{2\pi}E \\ -\frac{1}{\lambda}E \end{bmatrix} \in \mathbb{R}^{2m \times 3}.$$

Assuming coherent integration over T_{coh} and white Gaussian noise, the measurement noise covariance is

$$V_{\text{ultra}} = \frac{1}{2(C/N_0)_{\text{lin}} T_{\text{coh}}} I_{2m}.$$

In this work, we set $C/N_0 = 45$ dB-Hz and convert it to linear units as

$$(C/N_0)_{\text{lin}} = 10^{(C/N_0)_{\text{dB-Hz}}/10},$$

which is then used in V_{ultra} , with $T_{\text{coh}} = 10$ ms.

B. Tightly coupled model

For the tightly coupled architecture, the state vector includes receiver position and clock bias,

$$\mathbf{x} = [\delta \mathbf{r}^T \quad \delta(cdt)]^T \in \mathbb{R}^4.$$

The measurement vector stacks pseudorange and carrier-phase observations (expressed in meters),

$$\mathbf{z}_{\text{tight}} = [\delta \rho_1 \quad \cdots \quad \delta \rho_m \quad \delta \phi_1 \quad \cdots \quad \delta \phi_m]^T \in \mathbb{R}^{2m}.$$

Let $\mathbf{1} \in \mathbb{R}^{m \times 1}$ be a vector of ones. The measurement matrix is

$$H_{\text{tight}} = \begin{bmatrix} -E & -\mathbf{1} \\ -E & -\mathbf{1} \end{bmatrix} \in \mathbb{R}^{2m \times 4}.$$

The measurement noise covariance is modeled as

$$V_{\text{tight}} = \begin{bmatrix} \sigma_\rho^2 I_m & 0 \\ 0 & \sigma_\phi^2 I_m \end{bmatrix} \in \mathbb{R}^{2m \times 2m},$$

where σ_ρ and σ_ϕ denote the standard deviations of pseudorange and carrier-phase measurements, respectively. In this work, we set $\sigma_\rho = 1$ m and $\sigma_\phi = 0.005$ m.

C. Loosely coupled model

In the loosely coupled case, the GNSS position solution is treated as a direct measurement:

$$\mathbf{z}_{\text{loose}} = \delta \hat{\mathbf{r}} \in \mathbb{R}^3, \quad \delta \hat{\mathbf{r}} = I_3 \delta \mathbf{r} + \mathbf{v}.$$

The measurement Jacobian and covariance are

$$H_{\text{loose}} = [I_3 \quad 0_{3 \times 1}] \in \mathbb{R}^{3 \times 4}, \quad V_{\text{loose}} = \Sigma_{\text{pos}} \in \mathbb{R}^{3 \times 3},$$

where Σ_{pos} denotes the covariance of the GNSS position solution, often approximated as $\Sigma_{\text{pos}} = \sigma_{\text{pos}}^2 I_3$. In this work, we use $\sigma_{\text{pos}} = 1$ m.

ACKNOWLEDGEMENTS

This article is based on work supported by the Center for Assured and Resilient Navigation in Advanced TransportatION Systems (CARNATIONS) under the US Department of Transportation (USDOT)'s University Transportation Center (UTC) program (Grant No. 69A3552348324). Any opinions, findings, conclusions, or recommendations expressed in this paper are those of the authors and do not necessarily reflect the views of the sponsors.

REFERENCES

- Bar-Shalom, Y., Li, X.-R., and Kirubarajan, T. (2001). *Estimation with Applications to Tracking and Navigation*. John Wiley & Sons, New York.
- Falco, G., Pini, M., and Marucco, G. (2017). Loose and tight GNSS/INS integrations: Comparison of performance assessed in real urban scenarios. *Sensors*, 17(2):255.
- Groves, P. D. (2013). *Principles of GNSS, Inertial, and Multisensor Integrated Navigation Systems*. Artech House, Norwood, MA, 2 edition.
- Jwo, D.-J., Yang, C.-F., Chuang, C.-H., and Lin, K.-C. (2012). A novel design for the ultra-tightly coupled GPS/INS navigation system. *Journal of Navigation*, 65(4):717–747.
- Lashley, M., Bevely, D. M., and Hung, J. Y. (2009). Performance analysis of vector tracking algorithms for weak GPS signals in high dynamics. *IEEE Journal of Selected Topics in Signal Processing*, 3(4):661–673.
- Martin, S. M. (2023). Performance analysis of a RTK vector phase-locked loop architecture for GPS signal tracking in degraded environments. *NAVIGATION: Journal of the Institute of Navigation*, 70(4).
- Morales Ferre, R., de la Fuente, A., and Lohan, E.-S. (2019). Jammer classification in GNSS bands via machine learning algorithms. *Sensors*, 19(22):4841.
- Nagai, K., Spenko, M., Henderson, R., and Pervan, B. (2024). Fault-free integrity of urban driverless vehicle navigation with multi-sensor integration: A case study in downtown chicago. *NAVIGATION*, 71(1).
- Niu, X., Ban, Y., Zhang, Q., Zhang, T., Zhang, H., and Liu, J. (2015). Quantitative analysis to the impacts of IMU quality in GPS/INS deep integration. *Micromachines*, 6(8):1082–1099.
- Pany, T., Winkel, J., Riedl, B., Restle, M., Wörz, T., Schweikert, R., Niedermeier, H., Ameres, G., Eissfeller, B., Lagrasta, S., and López-Risuño, G. (2009). Performance of a partially coherent ultra-tightly coupled GNSS/INS pedestrian navigation system enabling coherent integration times of several seconds to track GNSS signals down to 1.5 dbhz. In *Proceedings of the 22nd International Technical Meeting of the Satellite Division of The Institute of Navigation (ION GNSS 2009)*, pages 919–934, Savannah, GA. Institute of Navigation.
- Parkinson, B. W. and Spilker, James J., J., editors (1996). *Global Positioning System: Theory and Applications, Volume I*, volume 163 of *Progress in Astronautics and Aeronautics*. American Institute of Aeronautics and Astronautics (AIAA), Washington, DC.
- Spilker, James J., J. (1977). *Digital Communications by Satellite*. Prentice-Hall Information Theory Series. Prentice-Hall.
- Watts, T. M. and Martin, S. M. (2022). Evaluation of cooperative vector tracking under multipath. In *Proceedings of the 2022 International Technical Meeting of The Institute of Navigation*, pages 980–1014, Long Beach, California.